Coupled dark sector models and cosmological tensions

Gang Liu,* Jiaze Gao, Yufen Han, Yuhao Mu, and Lixin Xu†

Institute of Theoretical Physics School of Physics Dalian University of Technology Dalian 116024, People's Republic of China

(Received 24 October 2023; revised 4 March 2024; accepted 26 April 2024; published 20 May 2024)

In this paper, we introduce two coupling models of early dark energy (EDE) and cold dark matter aimed at alleviating cosmological tensions. We utilize the EDE component in the coupling models to relieve the Hubble tension, while leveraging the interaction between dark matter and dark energy to alleviate the large-scale structure tension. The interaction is implemented in the form of pure momentum coupling and Yukawa coupling. We employed various cosmological datasets, including cosmic microwave background radiation, baryon acoustic oscillations, type Ia supernovae, the local distance-ladder data (SH0ES), and the Dark Energy Survey year-3 data, to analyze our models. We first *exclude* SH0ES data from the entire dataset to constrain the parameters of novel models. We observe that the values of H_0 obtained from two coupling models are 69.47 ± 0.71 km/s/Mpc and 69.65 ± 0.61 km/s/Mpc, respectively, at a 68% confidence level, slightly higher than that from the ΛCDM model, which is 68.21 ± 0.39 km/s/Mpc, but they exhibit a significant inconsistency with the SH0ES data, consistent with prior research findings in the EDE model. Subsequently, we incorporate SH0ES data to reconstrain the parameters of various models, our findings reveal that both coupling models yield best-fit values for H_0 approximately around 72.23 km/s/Mpc, which would alleviate the tension in the Hubble parameter. However, similar to the EDE model, the coupling models yield the S_8 values that still surpasses the result of the ΛCDM model. Nevertheless, the best-fit values for S_8 obtained with the two new models are 0.8192 and 0.8177, respectively, which are lower than the 0.8316 achieved by the EDE model. Consequently, although our coupling models fail to fully resolve the large-scale structure tension, they partially mitigate the adverse effect of the original EDE model.

DOI: 10.1103/PhysRevD.109.103531

I. INTRODUCTION

Despite the success of the ΛCDM model in explaining various cosmological data such as cosmic microwave background (CMB), baryon acoustic oscillation (BAO), and type Ia supernovae (SNIa), it does not provide insights into the nature of dark matter and dark energy. Furthermore, with the increasing precision and abundance of cosmological observations, inconsistencies between the concordance cosmological model and observational data have become more pronounced.

Among these disparities, the most renowned one is the Hubble tension, which refers to the inconsistency between the inferred value of the Hubble constant at high redshift based on CMB observations within the framework of the ΛCDM model, and the model-independent measured value of the Hubble constant at low redshift [1].

Based on the *Planck* 2018 CMB data, the ΛCDM model infers the Hubble constant value of 67.37 ± 0.54 km/s/Mpc [2]. However, utilizing the distance ladder method based on cepheid-calibrated SNIa data, the SH0ES measurement yields the Hubble constant value of 73.04 ± 1.04 km/s/Mpc [3], resulting in a statistical error of 4.8σ.

Another manifestation of a relatively mild tension concerns the contradiction between measurements of large-scale structure and CMB [4,5], typically described by $S_8 \equiv \sigma_8 \sqrt{(\Omega_\mathrm{m}/0.3)}$. Here, Ω_m represents the current total matter energy density fraction, while σ_8 denotes the root mean square of matter fluctuations at a scale of 8 h^{-1}Mpc. The *Planck* 2018 best-fit ΛCDM model predicts the S_8 value of 0.834 ± 0.016 [2]. However, measurements from large-scale structure, such as the Dark Energy Survey Year-3 (DES-Y3), yields the S_8 value of 0.776 ± 0.017 [6].

Various models have been proposed to address the issues concerning dark matter and dark energy. Commonly encountered models include various dynamical dark energy models [7–9], early dark energy [10–12], new early dark energy [13,14], decaying dark matter [15–18], interacting dark matter [19], axion dark matter [20,21], interacting dark energy [22,23] and so on.

One of the most intriguing models is the early dark energy (EDE) model [10–12]. By introducing an EDE component before recombination, it is possible to reduce

*liugang_dlut@mail.dlut.edu.cn
†lxxu@dlut.edu.cn

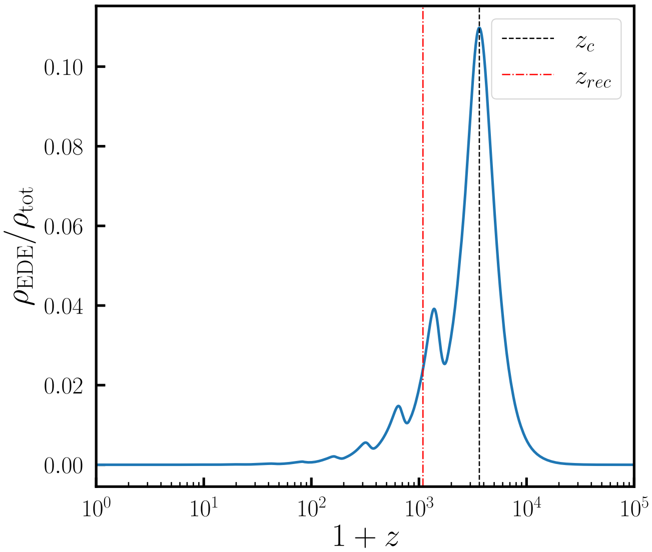

FIG. 1. The evolution of the energy density fraction of EDE with respect to redshift. The red dash-dotted line represents the recombination redshift, and it can be observed that the peak contribution of EDE occurs before recombination.

the comoving sound horizon of last scattering,

$$r_s(z_*) = \int_{z_*}^{\infty} \frac{c_s(z)}{H(z)} dz, \tag{1}$$

where z_* represents the redshift of last scattering, and c_s is the speed of sound of the photon-baryon plasma. This allows for an increase in H_0 while maintaining consistency with the CMB observations of angular scale of the sound horizon,

$$\theta_s = \frac{r_s(z_*)}{D_A(z_*)}, \tag{2}$$

where, $D_A(z_*)$ refers to the angular diameter distance to the last scattering.

EDE is typically described by an ultralight axion scalar field [24,25]. We denote the redshift corresponding to the peak contribution of EDE as z_c and the ratio of EDE energy density to the total energy density at this redshift as $f_{\rm EDE}$. Figure 1 illustrates the evolution of the EDE energy density fraction with redshift, where the red dash-dotted line represents the recombination redshift and the EDE contribution peak occurs earlier than recombination. The parameters used in the figure are shown in Eq. (30).

Despite the partially mitigation of the Hubble tension by the EDE model, it introduces additional issues. The EDE component suppresses the growth of perturbations during its contribution period, necessitating an increase in the cold dark matter density to remain consistent with CMB data. Furthermore, several other cosmological parameters, such as the scalar spectral index $n_{\rm s}$, baryon density $\omega_{\rm b}$, and amplitude of density fluctuations σ_8, undergo changes [26]. As a result, the EDE model further exacerbates the existing large-scale structure tension [11,27].

Our primary focus is on the EDE model whereby the interaction between dark matter and EDE is introduced to mitigate the adverse effect associated with the EDE model. Previous works have investigated various forms of interactions between dark matter and EDE [26,28–30]. In this paper, we discuss two forms of coupling, pure momentum coupling and Yukawa coupling.

The pure momentum interaction between dark matter and dark energy has been investigated in some previous coupled quintessence models [31–33]. In contrast to many previous phenomenological interacting dark energy models [34–37], the authors in [31] utilize the pull-back formalism to provide a generalized fluid action that includes scalar field couplings, where the *type 3* model correspond to theory of pure momentum transfer. In this investigation, we extend its application to the coupling between early dark energy and cold dark matter, proposing the momentum-coupled dark sector (MCDS) model.

The Yukawa coupling form was originally utilized to describe the interaction between pions and nucleons [38]. Here, we extend its application to characterize the interaction between dark matter and dark energy [39,40], where the scalar field represents the dark energy component, while the fermion field represents the dark matter component. We employ this form of interaction to construct the Yukawa-coupled dark sector (YCDS) model.

The EDE component in the coupling models is introduced to alleviate the Hubble tension, while the interaction between cold dark matter and EDE is employed to suppress the growth of matter structures and thereby alleviate large-scale structure tension.

The structure of this paper is organized as follows: In Sec. II, we present two coupling models and provide the background and perturbation evolution equations for EDE and cold dark matter. Section III presents the numerical results, including the impact on the Hubble parameter and matter power spectrum. In Sec. IV, we introduce the datasets used for the Monte Carlo Markov Chain analysis and present the constrained outcomes. Finally, in Sec. V, we summarize our findings.

II. TWO COUPLING DARK SECTOR MODELS

The action of early dark energy (EDE), cold dark matter, and interaction term can be represented as follows,

$$\mathcal{S} = \int d^4x\sqrt{-g}\Big[-\frac{1}{2}\partial^\mu\phi\partial_\mu\phi - V(\phi) \\ - i\bar{\psi}\not{D}\psi - m_\psi\bar{\psi}\psi + \mathcal{L}_{\rm int}\Big], \tag{3}$$

where ϕ represents the EDE scalar and ψ is the Dirac fermion that plays the role of cold dark matter, with m_ψ

denoting its mass. In the nonrelativistic limit, $\langle\bar{\psi}\psi\rangle \to n_\psi$, where n_ψ represents the number density. The energy-momentum tensor of cold dark matter can be expressed as,

$$T^{\mu}_{(c)\nu} = m_\psi n_\psi u^\mu u_\nu = \rho_c u^\mu u_\nu, \tag{4}$$

where u^μ and ρ_c denote the four-velocity and energy density of cold dark matter, respectively. We employ the subscript "$_c$" to symbolize cold dark matter in the subsequent discourse. We adopt the EDE potential form from [11,12],

$$V(\phi) = m_\phi^2 f_\phi^2 [1 - \cos(\phi/f_\phi)]^3 + V_\Lambda, \tag{5}$$

where m_ϕ denotes the axion mass, f_ϕ represents the decay constant, and V_Λ performs as the cosmological constant.

A. Momentum-coupled dark sector model

We have the flexibility to select the form of interactions in order to obtain various specific models. Following [31,32], we firstly focus on the following pure momentum coupling form,

$$\mathcal{L}_{\rm int} = -\beta(u^\mu \partial_\mu \phi)^2, \tag{6}$$

where β is a constant that describes the strength of the coupling. Consequently, the EDE and cold dark matter solely engage in momentum exchange.

By varying the action Eq. (3) with respect to the metric $g^{\mu\nu}$, we obtain the energy-momentum tensor for EDE and cold dark matter, including their interaction term, as follows,

$$\begin{aligned} T^{\mu}_{(\phi)\nu} + T^{\mu}_{(c)\nu} &= \partial^\mu\phi\partial_\nu\phi + \rho_c u^\mu u_\nu + 2\beta(u^\alpha\partial_\alpha\phi)(u^\mu\partial_\nu\phi) \\ &\quad - \delta^\mu{}_\nu\left[\frac{1}{2}\partial^\alpha\phi\partial_\alpha\phi + V(\phi) + \beta(u^\alpha\partial_\alpha\phi)^2\right], \end{aligned} \tag{7}$$

with $u^\mu = a^{-1}(1, v^i)$, $u_\mu = a(-1, v^i)$, where a denotes the scale factor and v^i is the three-velocity of cold dark matter. Due to the consideration of only the interaction between EDE and cold dark matter, the total energy-momentum tensor of both components is covariantly conserved,

$$\nabla_\mu (T^{\mu}_{(\phi)\nu} + T^{\mu}_{(c)\nu}) = 0. \tag{8}$$

We decompose the EDE scalar and the energy density of cold dark matter into their background and perturbation components,

$$\phi = \bar{\phi}(\tau) + \delta\phi(\tau, x^i), \tag{9a}$$

$$\rho_c = \bar{\rho}_c + \delta\rho_c = \bar{\rho}_c(1 + \delta_c), \tag{9b}$$

where τ represents conformal time.

1. Background equations

The variation of the action expanded to linear order in $\delta\phi$ yields the equation of motion for the scalar field background,

$$\bar{\phi}'' + 2\mathcal{H}\bar{\phi}' + \frac{a^2 V_\phi}{1 - 2\beta} = 0, \tag{10}$$

where the prime denotes the derivative with respect to conformal time τ, $\mathcal{H}$ is the conformal Hubble parameter, and V_ϕ denotes the partial derivative of the EDE potential with respect to $\bar{\phi}$.

By evaluating Eq. (8) at the background level and substituting the result of Eq. (10) into it, we obtain the energy density equation for cold dark matter,

$$\bar{\rho}_c' = -3\mathcal{H}\bar{\rho}_c. \tag{11}$$

If we define the energy density and pressure of momentum-coupled EDE in the following form,

$$\bar{\rho}_\phi = \frac{\bar{\phi}'^2}{2a^2}(1 - 2\beta) + V(\bar{\phi}), \tag{12a}$$

$$\bar{p}_\phi = \frac{\bar{\phi}'^2}{2a^2}(1 - 2\beta) - V(\bar{\phi}), \tag{12b}$$

the energy density equation for EDE is given by,

$$\bar{\rho}_\phi' = -3\mathcal{H}(\bar{\rho}_\phi + \bar{p}_\phi). \tag{13}$$

We can observe that the continuity equations for EDE and cold dark matter are consistent with their uncoupled forms. This is because we only consider the momentum exchange between EDE and cold dark matter, which only affects their velocity evolution equations.

In addition, by combining Eqs. (10) and (12), it can be inferred that the model is physically viable for $\beta < \frac{1}{2}$. When $\beta \to \frac{1}{2}$, a strong coupling issue arises. For $\beta > \frac{1}{2}$, the presence of a negative kinetic term leads to the inclusion of ghost in the theory [32].

2. Perturbation equations

We utilize the synchronous gauge to derive the perturbation equations for EDE and cold dark matter, the line element is defined as,

$$ds^2 = a^2(\tau)[-d\tau^2 + (\delta_{ij} + h_{ij})dx^i dx^j]. \tag{14}$$

The variation of the action expanded to quadratic order in $\delta\phi$ yields the equation of motion for the scalar field perturbation,

$$\delta\phi'' + 2\mathcal{H}\delta\phi' + \frac{1}{2}h'\bar{\phi}' + \frac{(k^2 + a^2 V_{\phi\phi})\delta\phi}{1 - 2\beta} - \frac{2\beta\bar{\phi}'\theta_c}{1 - 2\beta} = 0, \tag{15}$$

where $V_{\phi\phi}$ represents the second-order partial derivative of the EDE potential with respect to $\bar{\phi}$, and $\theta_c \equiv \partial_i v^i$ is the velocity divergence of cold dark matter.

According to Eq. (7), the density perturbation, pressure perturbation, and velocity divergence of momentum-coupled EDE are given by,

$$\delta\rho_\phi = \frac{\bar{\phi}'\delta\phi'}{a^2}(1-2\beta) + V_\phi \delta\phi, \tag{16a}$$

$$\delta p_\phi = \frac{\bar{\phi}'\delta\phi'}{a^2}(1-2\beta) - V_\phi \delta\phi, \tag{16b}$$

$$(\bar{\rho}_\phi + \bar{p}_\phi)\theta_\phi = \frac{\bar{\phi}'}{a^2}k^2\delta\phi(1-2\beta). \tag{16c}$$

By calculating Eq. (8) at the perturbation level, we obtain the density contrast and velocity evolution equations for cold dark matter,

$$\delta_c' + \theta_c + \frac{1}{2}h' = 0, \tag{17a}$$

$$\theta_c' + \mathcal{H}\theta_c = \frac{2\beta\mathcal{H}\bar{\phi}'}{a^2\bar{\rho}_c}(\bar{\phi}'\theta_c - k^2\delta\phi). \tag{17b}$$

It can be observed that the equation for the density contrast of cold dark matter is consistent with its uncoupled form, while the velocity equation is coupled with EDE. The coupled model indirectly affects the density contrast equation of cold dark matter by modifying its velocity equation, thereby suppressing the growth of structures and alleviating large-scale structure tension.

B. Yukawa-coupled dark sector model

We can also adopt the Yukawa interaction form to describe the coupling between EDE and cold dark matter,

$$\mathcal{L}_{\rm int} = -\kappa\phi\bar{\psi}\psi, \tag{18}$$

where κ represents the dimensionless Yukawa coupling constant that describes the strength of the interaction. We can absorb the interaction term into the potential term of the fermion field. Specifically, if we use the following transformation form,

$$\kappa = \xi\frac{m_\psi}{M_{pl}}, \tag{19}$$

where ξ is a dimensionless constant and M_{pl} represents the reduced Planck mass, then the mass of cold dark matter including the coupling term can be expressed as,

$$m_c = m_\psi + \kappa\phi = m_\psi\left(1 + \frac{\xi\phi}{M_{pl}}\right). \tag{20}$$

The energy density of cold dark matter is given by,

$$\rho_c = m_c n_\psi = \widetilde{\rho_c}\left(1 + \frac{\xi\phi}{M_{pl}}\right), \tag{21}$$

where $\tilde{\rho_c}$ represents the energy density of cold dark matter without interaction. We find that the Yukawa coupling of the dark sector is equivalent to the dependence of the cold dark matter energy density on the EDE scalar. Previous research has utilized the swampland conjecture [41,42] to propose a coupling form where the dark matter energy density exhibits exponential dependence on the EDE scalar [26,29]. The Yukawa coupling model can be regarded as a higher-order truncation of the exponential form.

1. Background equations

Expanding the action in Eq. (3) to linear order and carrying out the variation with respect to $\delta\phi$, we obtain the background evolution equation for the EDE scalar,

$$\bar{\phi}'' + 2\mathcal{H}\bar{\phi}' + a^2 V_\phi = -a^2 F\bar{\rho}_c, \tag{22}$$

where

$$F = \frac{\xi}{M_{pl} + \xi\bar{\phi}}. \tag{23}$$

By utilizing the conservation of the total energy-momentum tensor for dark matter and dark energy, in conjunction with Eqs. (8) and (22), we obtain the energy density equation for cold dark matter,

$$\bar{\rho}_c' + 3\mathcal{H}\bar{\rho}_c = \bar{\phi}' F\bar{\rho}_c. \tag{24}$$

The energy density and pressure of EDE are defined as follows [43],

$$\bar{\rho}_\phi = \frac{\bar{\phi}'^2}{2a^2} + V(\bar{\phi}), \tag{25a}$$

$$\bar{p}_\phi = \frac{\bar{\phi}'^2}{2a^2} - V(\bar{\phi}). \tag{25b}$$

Combining the Klein-Gordon equation for the EDE scalar field in Eq. (22), we obtain the energy density evolution equation for EDE,

$$\bar{\rho}_\phi' + 3\mathcal{H}(\bar{\rho}_\phi + \bar{p}_\phi) = -\bar{\phi}' F\bar{\rho}_c. \tag{26}$$

In Fig. 2, we illustrate the evolution with redshift of the ratio of EDE energy density to total energy density

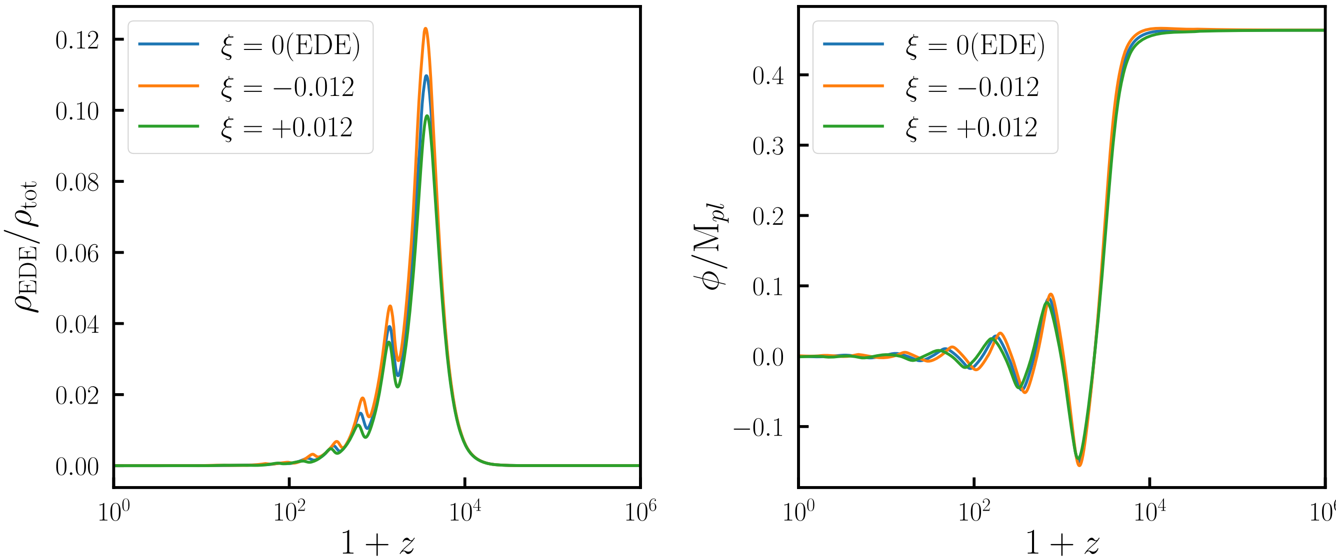

FIG. 2. The evolution with redshift of the EDE energy density fraction (left panel) and the EDE scalar (right panel) for various coupling constants is presented. The EDE energy density fraction and the amplitude and phase of the EDE scalar are affected by different coupling constants. A negative coupling constant leads to an increase in the EDE energy density fraction.

(left panel) and the EDE scalar (right panel) for different coupling constants. The remaining cosmological parameters are taken from Eq. (30). Different coupling constants lead to variations in the EDE energy density fraction and the amplitude and phase of the EDE scalar. The sign of the coupling constant determines the direction of energy density transfer between dark matter and dark energy. A negative coupling constant results in energy transfer from dark matter to dark energy, leading to a greater EDE energy density fraction, while the effect is reversed for a positive coupling constant.

2. *Perturbation equations*

Expanding the action to the quadratic order and taking the variation with respect to $\delta\phi$, we can derive the perturbation evolution equation for the EDE scalar,

$$\delta\phi'' + 2\mathcal{H}\delta\phi' + \frac{1}{2}h'\bar{\phi}' + (k^2 + a^2 V_{\phi\phi})\delta\phi = -a^2 F\bar{\rho}_c(\delta_c - F\delta\phi). \tag{27}$$

By exploiting the covariant conservation of the total energy-momentum tensor for cold dark matter and dark energy, we can derive the evolution equations for the density contrast and velocity divergence of cold dark matter,

$$\delta_c' + \theta_c + \frac{1}{2}h' = F(\delta\phi' - F\bar{\phi}'\delta\phi), \tag{28a}$$

$$\theta_c' + \mathcal{H}\theta_c = F(k^2\delta\phi - \bar{\phi}'\theta_c). \tag{28b}$$

C. Initial conditions

In the early universe, the Hubble friction in the scalar field dominates, leading to effective freezing of the EDE scalar, with the initial value of $\bar{\phi}'$ set to 0. We take the ratio of the initial values of $\bar{\phi}$ and the axion decay constant, $\alpha_i \equiv \bar{\phi}_i/f_\phi$, as the model parameter [11,12]. As for cold dark matter, the background evolution equations for the energy density of cold dark matter degenerate to the form of the noncoupled case. Hence, we do not alter the initial conditions for cold dark matter. When calculating the perturbation equations, we employ adiabatic initial conditions, keeping the initial conditions for cold dark matter unchanged, and referring to [12] for the initial conditions of EDE.

III. NUMERICAL RESULTS

Based on the description in the previous section, we made modifications to the publicly available Boltzmann code CLASS [44,45]. We have incorporated a new component of cold dark matter into the calculation of the velocity equation, accounting for the coupling effects. Furthermore, we retained the original cold dark matter component within CLASS and set $\Omega_{\rm cdm} = 10^{-6}$ to maintain consistency with the definition of the synchronous gauge.

We present numerical results with cosmological parameters adopted from Table IV in [26]. Specifically, for the ΛCDM model, we employ the following parameter values:

$$100\theta_s = 1.04202, \quad \omega_b = 0.02258, \quad \omega_c = 0.1176, \quad \ln(10^{10}A_s) = 3.041, \quad n_s = 0.9706, \quad \tau_{\rm reio} = 0.0535. \tag{29}$$

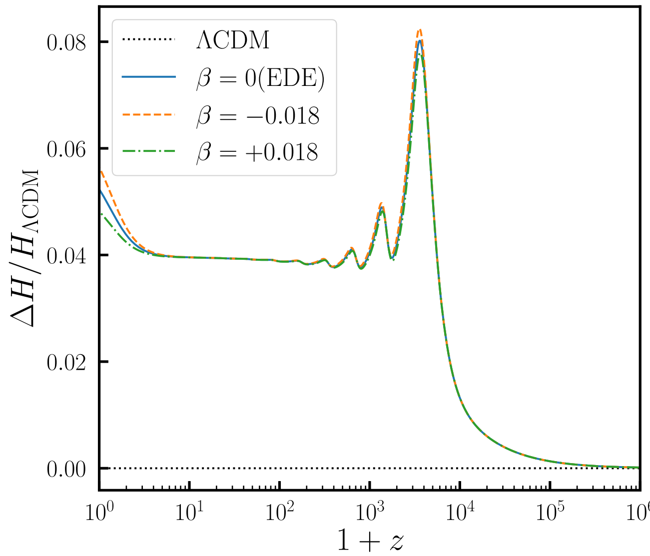

FIG. 3. The evolution of the Hubble parameter with redshift. The EDE component in the MCDS model enhances the Hubble parameter. A negative coupling parameter amplifies the effect of EDE, while positive coupling parameters weaken it.

For the two coupling models, we exclusively vary the values of the coupling parameters, while keeping the values of other cosmological parameters fixed to the constraints obtained from the EDE model,

$$\begin{aligned} 100\theta_s &= 1.04138, \quad \omega_b = 0.02281, \\ \omega_c &= 0.1287, \quad \ln(10^{10}A_s) = 3.065, \\ n_s &= 0.9895, \quad \tau_{\mathrm{reio}} = 0.0581, \quad \alpha_i = 2.77, \\ \log_{10}(f_\phi) &= 26.61, \quad \log_{10}(m_\phi) = -27.31. \end{aligned} \tag{30}$$

A. Momentum-coupled dark sector model

We demonstrate in Fig. 3 the impact of different values of the coupling parameter β in the MCDS model on the evolution of the Hubble parameter. The black dotted line represents the ΛCDM model, while the blue solid, orange dashed, and green dash-dotted lines represent the results for the MCDS model with coupling parameters 0, −0.018, and 0.018, respectively. It is worth noting that the MCDS model degenerates to the EDE model when the coupling parameter is set to 0.

It is evident that the EDE component in the MCDS model increases the Hubble parameter. Furthermore, a negative coupling parameter further enhances the Hubble parameter relative to the EDE model, while positive coupling parameters have the opposite effect. This phenomenon can be easily explained by the energy density formula for EDE in Eq. (12), where a negative coupling constant effectively amplifies the kinetic energy of EDE, resulting in an

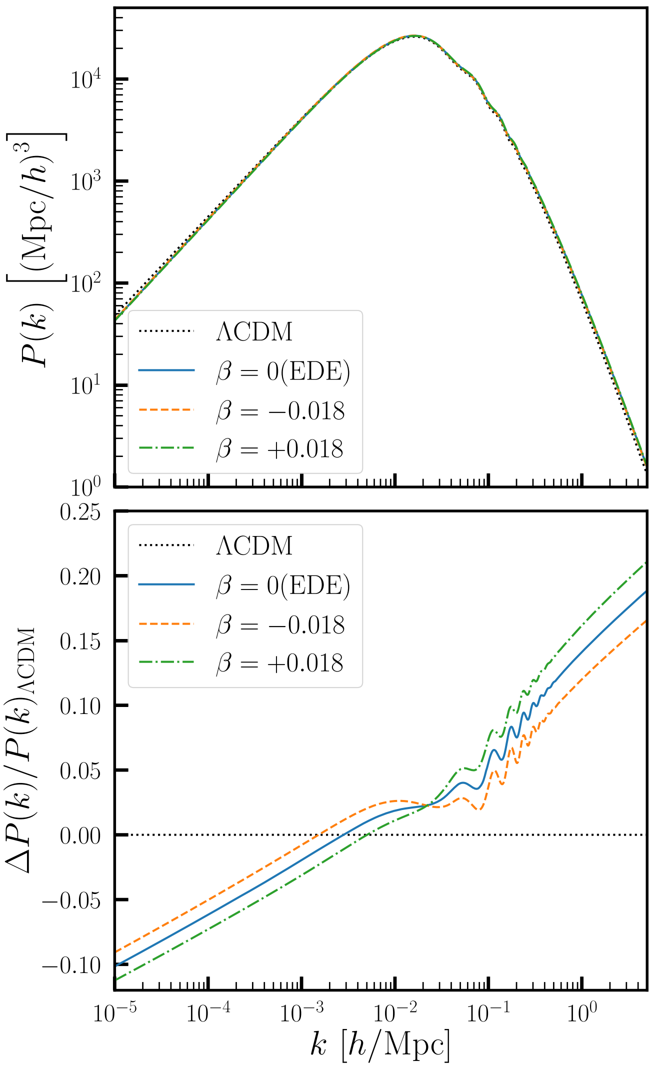

FIG. 4. The linear matter power spectra (upper panel) of the MCDS model with different coupling parameters, as well as the differences in power spectra relative to the ΛCDM model (lower panel), are depicted. Comparing with the EDE model (with the coupling constant of 0), a negative (positive) coupling constant reduces (increases) the power spectrum on small scales.

increased Hubble parameter. Conversely, positive coupling parameters diminish the Hubble parameter.

In Fig. 4, we showcase the linear matter power spectra of the MCDS model with different coupling parameters (upper panel) as well as the differences in power spectra relative to the ΛCDM model (lower panel).

It can be observed that the matter power spectrum of the momentum-coupled model still exceeds that of the ΛCDM model on small scales. However, the non-zero coupling constants result in momentum exchange between EDE and cold dark matter, which affects the velocity evolution equation of cold dark matter and indirectly impacts structure growth. Specifically, in comparison to the result of the EDE model (with the coupling constant of 0), a

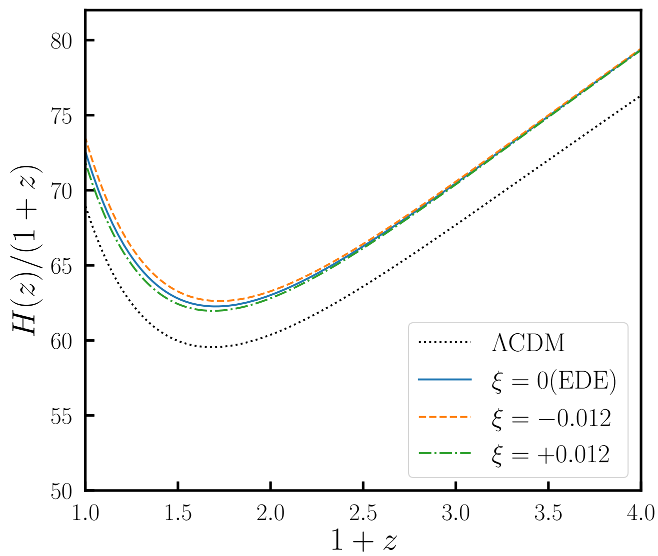

FIG. 5. The Hubble parameter evolves with redshift in the YCDS model. Different coupling constants impact the magnitude of the Hubble parameter based on the EDE model (with coupling constant $\xi = 0$). A negative value of the coupling constant increases the fraction of EDE energy density, thereby indirectly increasing H_0.

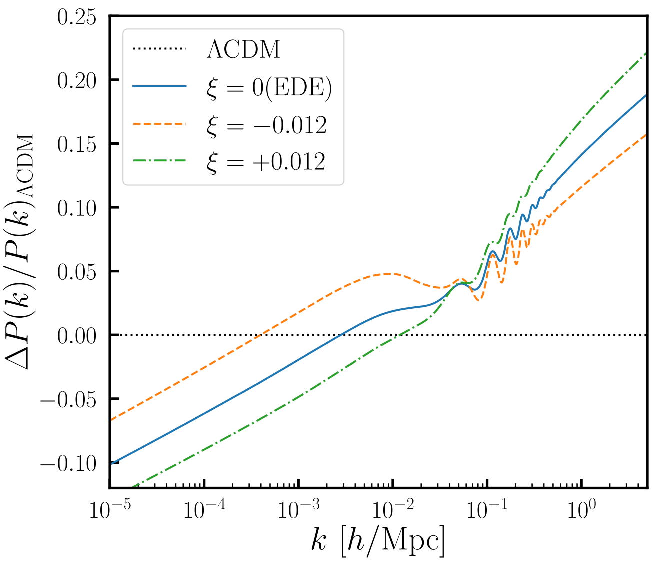

FIG. 6. The differences in the linear power spectrum relative to the ΛCDM model that arise from varying coupling constants in the YCDS model. A negative value of the coupling constant exhibits the reduction in the matter power spectrum on small scales, while a positive value of the coupling constant has the opposite effect.

negative coupling constant can decrease the power spectrum on small scales, thereby mitigating the negative effect in the original EDE model.

B. Yukawa-coupled dark sector model

Figure 5 presents the redshift evolution of the Hubble parameter for the YCDS model. The black dotted line represents the ΛCDM model, while the blue solid line, orange dashed line, and green dash-dotted line correspond to the YCDS model with coupling constants ξ set to 0, −0.12, and 0.12, respectively.

The inclusion of the EDE component in the YCDS model leads to a higher Hubble parameter compared to the ΛCDM model. The magnitude of the Hubble parameter is further influenced by different coupling constants based on the EDE model (with coupling constant $\xi = 0$). A negative coupling constant introduces source term in Eq. (26) for the evolution of the energy density of dark energy, leading to an increase in the EDE energy density fraction f_{EDE}, (as demonstrated by the influence of different coupling constants on the EDE energy density fraction illustrated in Fig. 2), thereby indirectly leading to an augmentation in the value of H_0. Conversely, positive value of the coupling constant yield the opposite effect.

In Fig. 6, we showcase the differences in power spectrum relative to the ΛCDM model when different coupling constants are taken in the YCDS model. The interaction between dark matter and dark energy affects the growth of matter structures and alters the shape of the power spectrum.

A negative value of the coupling constant corresponds to the transfer of energy density from dark matter to dark energy, reducing the amount of dark matter, together with the drag effect of dark energy on dark matter, this suppresses the clustering of matter and results in smaller $P(k)$ spectra on small scales compared to the original EDE model.

IV. DATA AND METHODOLOGY

We employ MontePython [46,47] to perform the Markov Chain Monte Carlo (MCMC) computations in order to obtain the posterior distribution of model parameters. The MCMC chains are analyzed using GetDist [48].

A. Datasets

In our MCMC analysis, we consider the following datasets:

(1) CMB: The temperature and polarization power spectra derived from the low-ℓ and high-ℓ measurements of the *Planck* 2018 data, along with the power spectrum of CMB lensing [2,49,50].
(2) BAO: The measurements acquired from the BOSS-DR12 $f\sigma_8$ sample encompass the combined LOWZ and CMASS galaxy samples [51,52], along with the low-redshift measurements derived from 6dFGS and the SDSS DR7 [53,54].
(3) Supernovae: The Pantheon dataset comprises 1048 type Ia supernovae with redshift values spanning from 0.01 to 2.3 [55].

TABLE I. By excluding the SH0ES data, the best-fit values and marginalized posterior probabilities at a 68% confidence level for parameter constraints of the ΛCDM model, EDE model, MCDS model, and YCDS model are obtained, using only CMB, BAO, SNIa, and S_8 measurements obtained from DES-Y3 data.

Model	ΛCDM	EDE	MCDS	YCDS
$\mathbf{100\omega_b}$	$2.249(2.252 \pm 0.014)$	$2.283(2.279 \pm 0.018)$	$2.276(2.272 \pm 0.016)$	$2.272(2.272 \pm 0.015)$
$\boldsymbol{\omega_c}$	$0.11823(0.11825 \pm 0.00085)$	$0.1232(0.1230^{+0.0020}_{-0.0023})$	$0.1228(0.1221^{+0.0017}_{-0.0025})$	$0.1232(0.1225^{+0.0018}_{-0.0024})$
$\boldsymbol{H_0}$	$68.11(68.21 \pm 0.39)$	$69.74(69.94^{+0.79}_{-0.49})$	$69.53(69.47 \pm 0.71)$	$69.51(69.65 \pm 0.61)$
$\mathbf{ln(10^{10}}\boldsymbol{A_s})$	$3.045(3.045 \pm 0.017)$	$3.060(3.055^{+0.015}_{-0.019})$	$3.050(3.049 \pm 0.016)$	$3.040(3.049 \pm 0.015)$
$\boldsymbol{n_s}$	$0.9699(0.9693 \pm 0.0038)$	$0.9845(0.9813^{+0.0056}_{-0.0048})$	$0.9794(0.9777 \pm 0.0058)$	$0.9766(0.9787 \pm 0.0047)$
$\boldsymbol{\tau_{reio}}$	$0.0568(0.0563 \pm 0.0080)$	$0.0594(0.0577^{+0.0081}_{-0.010})$	$0.0579(0.0563 \pm 0.0077)$	$0.0509(0.0555 \pm 0.0079)$
$\mathbf{log_{10}}(\boldsymbol{m_\phi})$	$\cdots$	$-26.837(-26.90^{+0.10}_{-0.081})$	$-26.824(-26.89^{+0.15}_{-0.12})$	$-26.920(-26.92^{+0.12}_{-0.067})$
$\mathbf{log_{10}}(\boldsymbol{f_\phi})$	$\cdots$	$26.392(26.405^{+0.081}_{-0.056})$	$26.381(26.348 \pm 0.079)$	$26.361(26.369^{+0.094}_{-0.11})$
$\boldsymbol{\alpha_i}$	$\cdots$	$2.845(2.81^{+0.10}_{-0.076})$	$2.843(2.80^{+0.10}_{-0.075})$	$2.806(2.76^{+0.13}_{-0.10})$
$\boldsymbol{\beta/\xi}$	$\cdots$	$\cdots$	$0.010(-0.0095 \pm 0.041)$	$-0.014(-0.011 \pm 0.018)$
$10^{-9}A_s$	$2.101(2.102 \pm 0.035)$	$2.132(2.122^{+0.032}_{-0.041})$	$2.112(2.109^{+0.031}_{-0.035})$	$2.091(2.110 \pm 0.032)$
$100\theta_s$	$1.04181(1.04204^{+0.00027}_{-0.00030})$	$1.04182(1.04183^{+0.00026}_{-0.00041})$	$1.04170(1.04182^{+0.00028}_{-0.00033})$	$1.04201(1.04185 \pm 0.00040)$
f_{EDE}	$\cdots$	$0.0548(0.056 \pm 0.018)$	$0.0508(0.044^{+0.016}_{-0.022})$	$0.0502(0.050^{+0.018}_{-0.021})$
$\log_{10}(z_c)$	$\cdots$	$3.810(3.780^{+0.050}_{-0.037})$	$3.820(3.784^{+0.082}_{-0.074})$	$3.761(3.767^{+0.066}_{-0.038})$
Ω_m	$0.3047(0.3040 \pm 0.0050)$	$0.3016(0.2995^{+0.0058}_{-0.0047})$	$0.3024(0.3015 \pm 0.0057)$	$0.3033(0.3007 \pm 0.0048)$
σ_8	$0.8055(0.8056 \pm 0.0065)$	$0.8216(0.8178 \pm 0.0079)$	$0.8174(0.8121 \pm 0.0092)$	$0.8121(0.8157^{+0.0067}_{-0.0076})$
S_8	$0.8118(0.8110 \pm 0.0093)$	$0.8237(0.817 \pm 0.010)$	$0.8206(0.814 \pm 0.011)$	$0.8165(0.817 \pm 0.010)$
χ^2_{tot}	3818.96	3822.28	3820.16	3820.40

TABLE II. The best-fit parameters and 68% confidence level marginalized constraints for the ΛCDM model, EDE model, MCDS model, and YCDS model are presented. The comprehensive dataset, including CMB, BAO, SNIa, SH0ES, and S_8 from DES-Y3, is utilized. The upper section of the table shows the cosmological parameters employed for MCMC sampling, while the lower section displays the derived parameters.

Model	ΛCDM	EDE	MCDS	YCDS
$\mathbf{100\omega_b}$	$2.260(2.263 \pm 0.014)$	$2.276(2.281^{+0.024}_{-0.020})$	$2.280(2.287 \pm 0.020)$	$2.268(2.278 \pm 0.021)$
$\boldsymbol{\omega_c}$	$0.11729(0.11725 \pm 0.00084)$	$0.1310(0.1299 \pm 0.0028)$	$0.1287(0.1290^{+0.0028}_{-0.0023})$	$0.1293(0.1289 \pm 0.0022)$
$\boldsymbol{H_0}$	$68.64(68.71^{+0.35}_{-0.41})$	$71.85(72.46 \pm 0.86)$	$72.23(72.20^{+0.93}_{-0.80})$	$72.23(72.19^{+0.78}_{-0.70})$
$\mathbf{ln(10^{10}}\boldsymbol{A_s})$	$3.047(3.050 \pm 0.015)$	$3.057(3.063^{+0.015}_{-0.017})$	$3.065(3.064 \pm 0.015)$	$3.064(3.063 \pm 0.016)$
$\boldsymbol{n_s}$	$0.9733(0.9722 \pm 0.0040)$	$0.9877(0.9908 \pm 0.0059)$	$0.9898(0.9906^{+0.0057}_{-0.0051})$	$0.9849(0.9891^{+0.0053}_{-0.0048})$
$\boldsymbol{\tau_{reio}}$	$0.0576(0.0592 \pm 0.0082)$	$0.0539(0.0563 \pm 0.0090)$	$0.0565(0.0562 \pm 0.0074)$	$0.0572(0.0571^{+0.0073}_{-0.0086})$
$\mathbf{log_{10}}(\boldsymbol{m_\phi})$	$\cdots$	$-27.292(-27.290 \pm 0.055)$	$-27.292(-27.286^{+0.049}_{-0.60})$	$-27.333(-27.293^{+0.051}_{-0.062})$
$\mathbf{log_{10}}(\boldsymbol{f_\phi})$	$\cdots$	$26.632(26.616^{+0.056}_{-0.033})$	$26.609(26.602^{+0.047}_{-0.034})$	$26.630(26.613 \pm 0.034)$
$\boldsymbol{\alpha_i}$	$\cdots$	$2.762(2.783 \pm 0.069)$	$2.772(2.774^{+0.067}_{-0.051})$	$2.722(2.738^{+0.076}_{-0.054})$
$\boldsymbol{\beta/\xi}$	$\cdots$	$\cdots$	$-0.001(-0.006 \pm 0.014)$	$-0.012(-0.009 \pm 0.016)$
$10^{-9}A_s$	$2.105(2.112 \pm 0.032)$	$2.127(2.139^{+0.031}_{-0.036})$	$2.142(2.141 \pm 0.031)$	$2.141(2.140^{+0.032}_{-0.036})$
$100\theta_s$	$1.04206(1.04217^{+0.00025}_{-0.00031})$	$1.04121(1.04145 \pm 0.00043)$	$1.04172(1.04150 \pm 0.00038)$	$1.04126(1.04149 \pm 0.00035)$
f_{EDE}	$\cdots$	$0.1183(0.119^{+0.023}_{-0.018})$	$0.1100(0.111^{+0.022}_{-0.014})$	$0.1181(0.114 \pm 0.018)$
$\log_{10}(z_c)$	$\cdots$	$3.571(3.568 \pm 0.034)$	$3.570(3.571 \pm 0.029)$	$3.548(3.568^{+0.029}_{-0.035})$
Ω_m	$0.2983(0.2977 \pm 0.0048)$	$0.2991(0.2923 \pm 0.0056)$	$0.2915(0.2927^{+0.0061}_{-0.0051})$	$0.2925(0.2924 \pm 0.0052)$
σ_8	$0.8039(0.8047 \pm 0.0060)$	$0.8329(0.8325 \pm 0.0083)$	$0.8310(0.8294^{+0.0085}_{-0.0072})$	$0.8281(0.8305 \pm 0.0078)$
S_8	$0.8016(0.8016^{+0.0096}_{-0.0080})$	$0.8316(0.822^{+0.011}_{-0.0093})$	$0.8192(0.819^{+0.011}_{-0.0087})$	$0.8177(0.820^{+0.012}_{-0.0087})$
χ^2_{tot}	3838.20	3826.46	3825.94	3823.86
ΔAIC	$\cdots$	−5.74	−4.26	−6.34

Through the amalgamation of CMB and BAO data, multiple acoustic horizon measurements can be made at different redshifts, thereby alleviating geometric degeneracies and limiting the physical processes between recombination and the BAO measurement redshift. Furthermore, the supernova data obtained from the Pantheon sample exerts a substantial constraint on new physics specific to the late epoch within the redshift range that is measured.

(4) SH0ES: The most recent SH0ES measurement has estimated the value of the Hubble constant as 73.04 ± 1.04 km/s/Mpc [3].

We utilize the H_0 measurements obtained from SH0ES to mitigate the influence of the prior volume effect [56] and evaluate the effectiveness of the novel model in addressing the tension between the local measurement of H_0 and the inference results from CMB analysis.

(5) DES-Y3: Dark Energy Survey Year-3 weak lensing and galaxy cluster data, with a Gaussian constraint on S_8 of 0.776 ± 0.017 [6].

We incorporate the S_8 data from DES-Y3 to investigate how well the model performs in alleviating the large-scale structure tension. Previous studies have validated the effectiveness of using the S_8 prior approach to approximate DES-Y1 data in the context of EDE [11]. In this study, we assume that the S_8 prior remains a good approximation when using DES-Y3 data for the EDE model. Additionally, we propose two coupling dark sector models that exhibit only minor deviations from the EDE model, as demonstrated by the subsequent parameter constraints. Therefore, we anticipate that the S_8 prior approximation is applicable to the mentioned models in this paper, at least at the level of marginalized one-dimensional and two-dimensional posterior probability distributions [26].

B. Results

In order to assess the consistency among different datasets, we first examine the fitting performance of various models on all datasets *except* for SH0ES. The results are presented in Table I. The upper section of the table displays the parameters used for the MCMC sampling, while the lower section presents the derived parameters.

We observed that the constraints from the two coupling models closely align with those of the EDE model, yielding a slightly larger value for H_0 compared to the ΛCDM model's results. However, all models exhibit clear inconsistencies with the SH0ES data, consistent with previous research on EDE [11].

Subsequently, we incorporated the SH0ES data and reconstrained various models. The parameter constraint results for the ΛCDM model, the EDE model, the MCDS model, and the YCDS model are presented in Table II. We

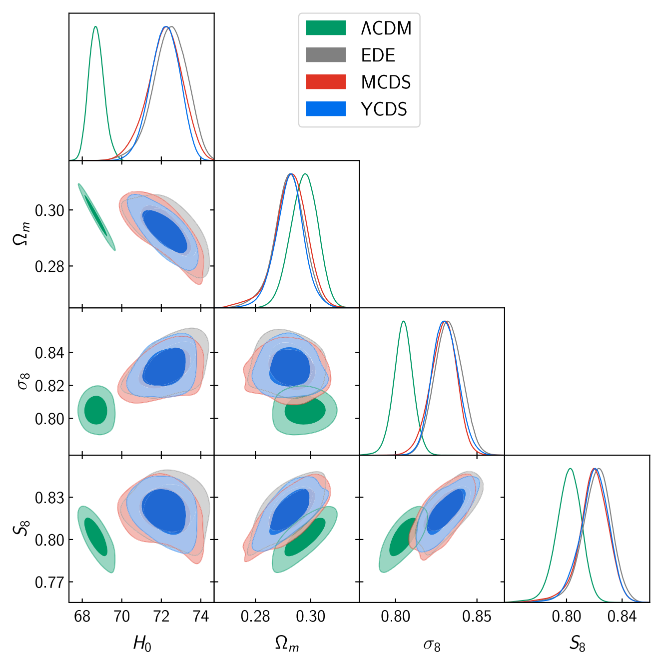

FIG. 7. Posterior distribution plot for selected parameters in the four models are presented. The MCDS model and YCDS model exhibit larger values of H_0 and S_8 relative to the ΛCDM model, thereby alleviating the Hubble tension while exacerbating the large-scale structure tension. However, the S_8 values of the two coupling models are smaller than that of the EDE model, partially mitigating the negative effect of the EDE model.

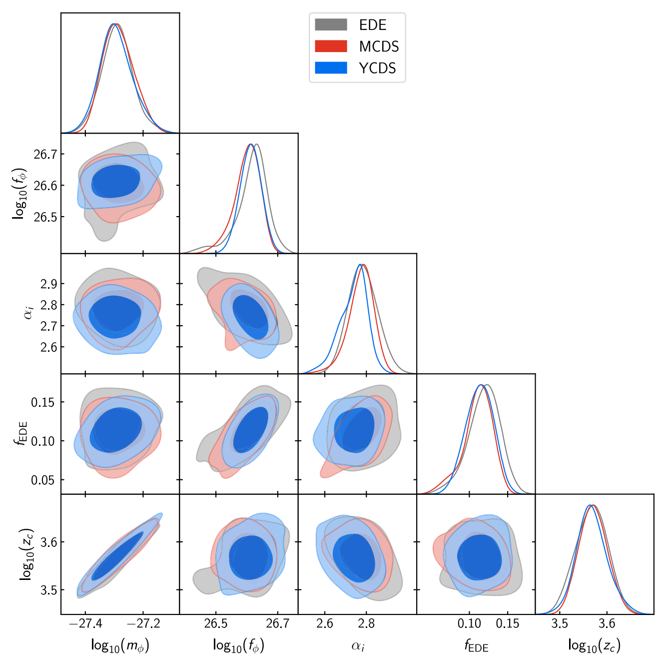

FIG. 8. The posterior distributions of the EDE parameters for the EDE model and the two coupling models are shown. The results from these three models are remarkably consistent, with only minor deviations observed in the results of the coupling models compared to those of the EDE model.

employed the complete dataset, including CMB, BAO, SNIa, SH0ES, and S_8 from DES-Y3 data.

We constrain the coupling constant β (ξ) to be -0.006 ± 0.014 (-0.009 ± 0.016) at a 68% confidence level. This indicates a weak interaction between EDE and cold dark matter. The negative coupling constants align with our expectations, effectively increasing H_0 and reducing the matter power spectrum on small scales, as discussed in Sec. III.

The constrained values of H_0 for the MCDS model and the YCDS model are $72.20^{+0.93}_{-0.80}$ km/s/Mpc and $72.19^{+0.78}_{-0.70}$ km/s/Mpc, respectively, at a 68% confidence level, both exceeding the value of $68.71^{+0.35}_{-0.41}$ km/s/Mpc for the ΛCDM model. This indicates that our coupling models inherit the ability of the EDE model to alleviate the Hubble tension.

However, the S_8 values constrained by the MCDS model and YCDS model are 0.8192 and 0.8177, respectively, which exacerbate the large-scale structure tension compared to the ΛCDM model's result of 0.8016. Nevertheless, the two coupling models have smaller S_8 values than the EDE model's result of 0.8316, partially mitigating the adverse effect caused by EDE.

Figure 7 illustrates the posterior distribution plot for selected parameters in the four models (for complete posterior distributions, please refer to Fig. 9 in the Appendix), revealing the noticeable increase in both H_0 and S_8 for the MCDS and YCDS models relative to the ΛCDM model.

In addition, the interaction between dark matter and dark energy in the coupling models inhibit structure growth, thereby reducing the clustering effects of matter. Consequently, the MCDS model and the YCDS model result in smaller values of S_8 compared to the EDE model.

In Fig. 8, we present the posterior distributions of the EDE parameters for the EDE model and the two coupling models. We find that the results from these three models are remarkably consistent. In fact, the results for other cosmological parameters in the coupling models are also close to those of the EDE model, with only minor deviations.

The penultimate row of Table II displays the $\chi^2_{\rm tot}$ values of different models. It can be observed that the $\chi^2_{\rm tot}$ values for the EDE model, MCDS model, and YCDS model are both smaller than that of the ΛCDM model, with the $\Delta\chi^2_{\rm tot}$ values of −11.74, −12.26, and −14.34 respectively, primarily driven by the SH0ES data. The $\chi^2_{\rm tot}$ value of the MCDS model and YCDS model are smaller than that of the EDE model, owing to the S_8 data from DES-Y3.

We also calculated the Akaike information criterion (AIC) to compare the models [57],[1]

$$\mathrm{AIC} = \chi^2_{\rm tot} + 2k, \tag{31}$$

where k represents the number of fitting parameters. The AIC values for the EDE model, MCDS model, and YCDS model relative to the ΛCDM model are displayed in the final row of Table II, which are −5.74, −4.26, and −6.34, respectively. Although the $\chi^2_{\rm tot}$ value of the MCDS model is smaller than that of the EDE model, the introduction of a new parameter results in a higher AIC value. The AIC value for the YCDS model is the smallest, indicating that, from the perspective of AIC, the YCDS model performs the best.

To quantify the level of tension using the SH0ES data, we calculated the following tension metric (in units of Gaussian σ) [58,59],

$$Q_{\rm DMAP} \equiv \sqrt{\chi^2(w/\mathrm{SH0ES}) - \chi^2(w/o\mathrm{SH0ES})}, \tag{32}$$

which involves the disparity in χ^2 when considering the data with and without SH0ES. This metric effectively captures the non-Gaussian nature of the posterior distribution. The tension metric yields results of 4.4σ, 2.1σ, 2.4σ, and 1.9σ for the ΛCDM model, EDE model, MCDS model, and YCDS model, respectively. Based on this criterion, we consider the performance of the EDE model and the two coupling models to be superior to that of the ΛCDM model, with the YCDS model exhibiting the best performance.

V. CONCLUSIONS

In this paper, we consider the interaction between early dark energy (EDE) and cold dark matter, proposing the momentum-coupled dark sector (MCDS) model and the Yukawa-coupled dark sector (YCDS) model to alleviate the Hubble tension and large-scale structure tension. The EDE component in the two coupling models is employed to alleviate the Hubble tension, while the momentum (or energy and momentum) exchange between EDE and cold dark matter can affect the evolution of cold dark matter density perturbation, thereby suppressing structure growth and mitigating large-scale structure tension.

We investigate the evolution equations of the background and perturbation for the coupled models, along with providing the corresponding initial conditions. We discuss the modifications to the original EDE model due to the momentum and Yukawa couplings between EDE and cold dark matter, as well as its effect on structure growth and matter power spectrum. Subsequently, we utilize various cosmological data, including CMB, BAO, SNIa, SH0ES, and S_8 from DES-3, to constrain the ΛCDM model, EDE model, MCDS model, and YCDS model.

We obtain the coupling constant β (ξ) to be -0.006 ± 0.014 (-0.009 ± 0.016) at a 68% confidence level, the negative coupling constants can suppress structure growth on small scales, aiding in alleviating the large-scale structure tension. The values for H_0 in the MCDS

[1]In fact, the utilization of Bayesian evidence for model selection is preferable. AIC often tends to favor overly complex models, particularly in cases of small sample sizes or high noise levels. However, due to the complexity involved in computing Bayesian evidence, we opt to employ the AIC in this study.

model and YCDS model are $72.20^{+0.93}_{-0.80}$ km/s/Mpc and $72.19^{+0.78}_{-0.70}$ km/s/Mpc, respectively, at a 68% confidence level, both models can alleviate the Hubble tension.

Meanwhile, the constrained values of S_8 in the two coupling models are 0.8192 and 0.8177, respectively, exceeding the results of the ΛCDM model, further exacerbating the large-scale structure tension. However, the interaction between EDE and cold dark matter in the MCDS model and the YCDS model lead to smaller values of S_8 compared to the EDE model's result of 0.8316, partially mitigating the negative effect of the original EDE model.

We compared the χ^2_{tot} values of different models, where the χ^2_{tot} values for the EDE model, MCDS model, and YCDS model relative to the ΛCDM model are −11.74, −12.26, and −14.34, respectively. The YCDS model exhibited the lowest χ^2_{tot} value. Additionally, we calculated the AIC for model comparison, with the results being −5.74, −4.26, and −6.34 for the EDE model, MCDS model, and YCDS model relative to the ΛCDM model, respectively. The YCDS model exhibits the smallest AIC value, indicating that, based on the AIC, it delivers the best performance among the models considered.

The two coupling models preserve the partially mitigation of the Hubble tension achieved by the EDE model, but they still fall short of completely resolving the large-scale structure tension. However, the couplings between EDE and cold dark matter alleviate the negative effect of the original EDE model, resulting in a smaller S_8 compared to the EDE model. Further research is needed to fully address the cosmological tensions.

ACKNOWLEDGMENTS

This work is supported in part by National Natural Science Foundation of China under Grants No. 12075042 and 11675032 (People's Republic of China).

APPENDIX: THE FULL MCMC POSTERIORS

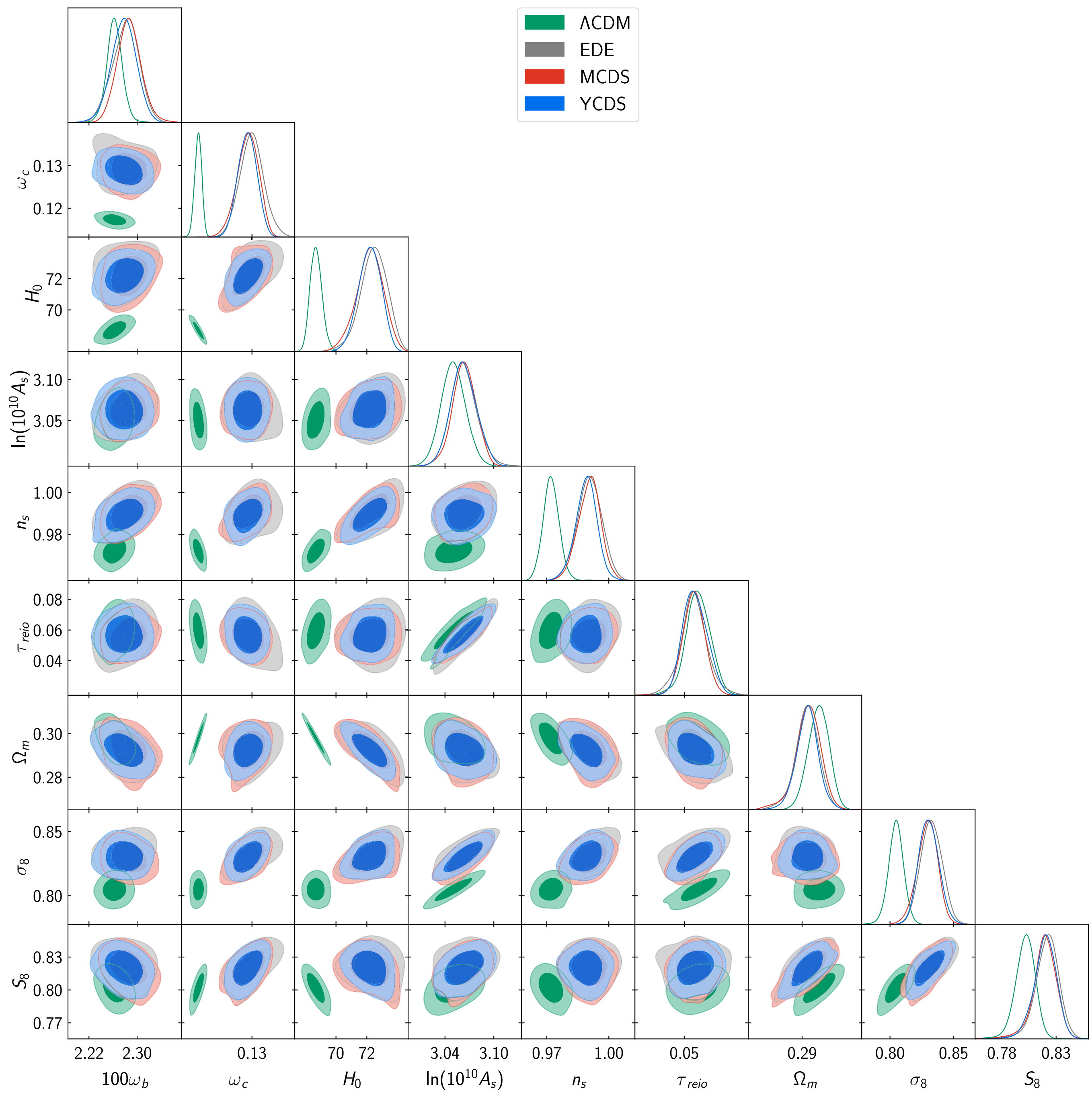

FIG. 9. The comprehensive posterior distributions for the ΛCDM, EDE, MCDS, and YCDS models are provided, utilizing data encompassing CMB, BAO, SNIa, SH0ES, and S_8 from DES-Y3.

[1] L. Verde, T. Treu, and A. G. Riess, Tensions between the early and late universe, Nat. Astron. **3**, 891 (2019).
[2] N. Aghanim, Y. Akrami *et al.* (Planck Collaboration), Planck 2018 results—VI. Cosmological parameters, Astron. Astrophys. **641**, A6 (2020).
[3] A. G. Riess, W. Yuan, L. M. Macri *et al.*, A comprehensive measurement of the local value of the Hubble constant with 1 km/s/Mpc uncertainty from the Hubble space telescope and the SH0ES team, Astrophys. J. Lett. **934**, L7 (2022).
[4] E. Macaulay, I. K. Wehus, and H. K. Eriksen, Lower growth rate from recent redshift space distortion measurements than expected from Planck, Phys. Rev. Lett. **111**, 161301 (2013).
[5] H. Hildebrandt, F. Köhlinger, J. Busch *et al.*, Kids+viking-450: Cosmic shear tomography with optical and infrared data, Astron. Astrophys. **633**, A69 (2020).
[6] T. M. C. Abbott, M. Aguena, A. Alarcon *et al.*, Dark Energy Survey year 3 results: Cosmological constraints from galaxy clustering and weak lensing, Phys. Rev. D **105**, 023520 (2022).
[7] R.-Y. Guo, J.-F. Zhang, and X. Zhang, Can the h0 tension be resolved in extensions to LCDM cosmology?, J. Cosmol. Astropart. Phys. 02 (2019) 054.
[8] X. Li and A. Shafieloo, A simple phenomenological emergent dark energy model can resolve the Hubble tension, Astrophys. J. Lett. **883**, L3 (2019).
[9] Z. Zhou, G. Liu, Y. Mu, and L. Xu, Can phantom transition at $z \sim 1$ restore the cosmic concordance?, Mon. Not. R. Astron. Soc. **511**, 595 (2022).
[10] V. Poulin, T. L. Smith, T. Karwal, and M. Kamionkowski, Early dark energy can resolve the Hubble tension, Phys. Rev. Lett. **122**, 221301 (2019).
[11] J. C. Hill, E. McDonough, M. W. Toomey, and S. Alexander, Early dark energy does not restore cosmological concordance, Phys. Rev. D **102**, 043507 (2020).
[12] T. L. Smith, V. Poulin, and M. A. Amin, Oscillating scalar fields and the Hubble tension: A resolution with novel signatures, Phys. Rev. D **101**, 063523 (2020).
[13] F. Niedermann and M. S. Sloth, New early dark energy, Phys. Rev. D **103**, L041303 (2021).
[14] F. Niedermann and M. S. Sloth, Resolving the Hubble tension with new early dark energy, Phys. Rev. D **102**, 063527 (2020).
[15] J. Buch, P. Ralegankar, and V. Rentala, Late decaying 2-component dark matter scenario as an explanation of the AMS-02 positron excess, J. Cosmol. Astropart. Phys. 10 (2017) 028.
[16] T. Bringmann, F. Kahlhoefer, K. Schmidt-Hoberg, and P. Walia, Converting nonrelativistic dark matter to radiation, Phys. Rev. D **98**, 023543 (2018).
[17] S. J. Clark, K. Vattis, and S. M. Koushiappas, Cosmological constraints on late-universe decaying dark matter as a solution to the H_0 tension, Phys. Rev. D **103**, 043014 (2021).
[18] S. Alvi, T. Brinckmann, M. Gerbino, M. Lattanzi, and L. Pagano, Do you smell something decaying? Updated linear constraints on decaying dark matter scenarios, J. Cosmol. Astropart. Phys. 11 (2022) 015.
[19] Z. Zhou, G. Liu, Y. Mu, and L. Xu, Limit on the dark matter mass from its interaction with photons, Phys. Rev. D **105**, 103509 (2022).
[20] F. D'Eramo, R. Z. Ferreira, A. Notari, and J. L. Bernal, Hot axions and the h0 tension, J. Cosmol. Astropart. Phys. 11 (2018) 014.
[21] G. Liu, Y. Mu, Z. Zhou, and L. Xu, Cosmological constraints on thermal friction of axion dark matter, Phys. Rev. D **108**, 123546 (2023).
[22] W. Yang, S. Pan, L. Xu, and D. F. Mota, Effects of anisotropic stress in interacting dark matter-dark energy scenarios, Mon. Not. R. Astron. Soc. **482**, 1858 (2018).
[23] E. D. Valentino, A. Melchiorri, O. Mena, and S. Vagnozzi, Interacting dark energy in the early 2020s: A promising solution to the H_0 and cosmic shear tensions, Phys. Dark Universe **30**, 100666 (2020).
[24] M. Kamionkowski, J. Pradler, and D. G. E. Walker, Dark energy from the string axiverse, Phys. Rev. Lett. **113**, 251302 (2014).
[25] D. J. Marsh, Axion cosmology, Phys. Rep. **643**, 1 (2016), axion cosmology.
[26] E. McDonough, M.-X. Lin, J. C. Hill, W. Hu, and S. Zhou, Early dark sector, the Hubble tension, and the swampland, Phys. Rev. D **106**, 043525 (2022).
[27] G. D'Amico, L. Senatore, P. Zhang, and H. Zheng, The Hubble tension in light of the full-shape analysis of large-scale structure data, J. Cosmol. Astropart. Phys. 05 (2021) 072.
[28] M.-X. Lin, E. McDonough, J. C. Hill, and W. Hu, Dark matter trigger for early dark energy coincidence, Phys. Rev. D **107**, 103523 (2023).
[29] G. Liu, Z. Zhou, Y. Mu, and L. Xu, Alleviating cosmological tensions with a coupled scalar fields model, Phys. Rev. D **108**, 083523 (2023).
[30] G. Liu, Z. Zhou, Y. Mu, and L. Xu, Kinetically coupled scalar fields model and cosmological tensions, Mon. Not. R. Astron. Soc. **529**, 1852 (2024).
[31] A. Pourtsidou, C. Skordis, and E. J. Copeland, Models of dark matter coupled to dark energy, Phys. Rev. D **88**, 083505 (2013).
[32] A. Pourtsidou and T. Tram, Reconciling CMB and structure growth measurements with dark energy interactions, Phys. Rev. D **94**, 043518 (2016).
[33] F. N. Chamings, A. Avgoustidis, E. J. Copeland, A. M. Green, and A. Pourtsidou, Understanding the suppression of structure formation from dark matter-dark energy momentum coupling, Phys. Rev. D **101**, 043531 (2020).
[34] G. Caldera-Cabral, R. Maartens, and B. M. Schaefer, The growth of structure in interacting dark energy models, J. Cosmol. Astropart. Phys. 07 (2009) 027.
[35] K. Koyama, R. Maartens, and Y.-S. Song, Velocities as a probe of dark sector interactions, J. Cosmol. Astropart. Phys. 10 (2009) 017.
[36] M. Benetti, W. Miranda, H. Borges, C. Pigozzo, S. Carneiro, and J. Alcaniz, Looking for interactions in the cosmological dark sector, J. Cosmol. Astropart. Phys. 12 (2019) 023.
[37] J. Beltrán Jiménez, D. Bettoni, D. Figueruelo, F. A. Teppa Pannia, and S. Tsujikawa, Probing elastic interactions in the dark sector and the role of S_8, Phys. Rev. D **104**, 103503 (2021).
[38] H. Yukawa, On the interaction of elementary particles. I, Prog. Theor. Phys. Suppl. **1**, 1 (1955).

[39] G. R. Farrar and P. J. E. Peebles, Interacting dark matter and dark energy, Astrophys. J. **604**, 1 (2004).

[40] M. Archidiacono, E. Castorina, D. Redigolo, and E. Salvioni, Unveiling dark fifth forces with linear cosmology, J. Cosmol. Astropart. Phys. 10 (2022) 074.

[41] C. Vafa, The string landscape and the swampland, arXiv: 0509212.

[42] E. Palti, The swampland: Introduction and review, Fortschr. Phys. **67**, 1900037 (2019).

[43] P. G. Ferreira and M. Joyce, Cosmology with a primordial scaling field, Phys. Rev. D **58**, 023503 (1998).

[44] D. Blas, J. Lesgourgues, and T. Tram, The cosmic linear anisotropy solving system (CLASS). Part II: Approximation schemes, J. Cosmol. Astropart. Phys. 07 (2011) 034.

[45] J. Lesgourgues, The cosmic linear anisotropy solving system (CLASS) I: Overview, arXiv:1104.2932.

[46] B. Audren, J. Lesgourgues, K. Benabed, and S. Prunet, Conservative constraints on early cosmology with MONTEPYTHON, J. Cosmol. Astropart. Phys. 02 (2013) 001.

[47] T. Brinckmann and J. Lesgourgues, Montepython 3: Boosted MCMC sampler and other features, Phys. Dark Universe **24**, 100260 (2019).

[48] A. Lewis, Getdist: A Python package for analysing Monte Carlo samples, arXiv:1910.13970.

[49] N. Aghanim, Y. Akrami, M. Ashdown *et al.*, Planck 2018 results. V. CMB power spectra and likelihoods, Astron. Astrophys. **641**, A5 (2020).

[50] N. Aghanim, Y. Akrami, M. Ashdown *et al.*, Planck 2018 results—VIII. Gravitational lensing, Astron. Astrophys. **641**, A8 (2020).

[51] S. Alam, M. Ata, S. Bailey *et al.*, The clustering of galaxies in the completed SDSS-III baryon oscillation spectroscopic survey: Cosmological analysis of the DR12 galaxy sample, Mon. Not. R. Astron. Soc. **470**, 2617 (2017).

[52] M. A. Buen-Abad, M. Schmaltz, J. Lesgourgues, and T. Brinckmann, Interacting dark sector and precision cosmology, J. Cosmol. Astropart. Phys. 01 (2018) 008.

[53] F. Beutler, C. Blake, M. Colless, D. H. Jones, L. Staveley-Smith, L. Campbell, Quentin Parker, W. Saunders, and Fred Watson, The 6df galaxy survey: Baryon acoustic oscillations and the local Hubble constant, Mon. Not. R. Astron. Soc. **416**, 3017 (2011).

[54] A. J. Ross, L. Samushia, C. Howlett, W. J. Percival, A. Burden, and M. Manera, The clustering of the SDSS DR7 main galaxy sample-i. a 4 percent distance measure at $z = 0.15$, Mon. Not. R. Astron. Soc. **449**, 835 (2015).

[55] D. M. Scolnic, D. O. Jones, A. Rest, Y. C. Pan *et al.*, The complete light-curve sample of spectroscopically confirmed SNe ia from pan-STARRS1 and cosmological constraints from the combined pantheon sample, Astrophys. J. **859**, 101 (2018).

[56] T. L. Smith, V. Poulin, J. L. Bernal, K. K. Boddy, M. Kamionkowski, and R. Murgia, Early dark energy is not excluded by current large-scale structure data, Phys. Rev. D **103**, 123542 (2021).

[57] H. Akaike, A new look at the statistical model identification, IEEE Trans. Autom. Control **19**, 716 (1974).

[58] M. Raveri and W. Hu, Concordance and discordance in cosmology, Phys. Rev. D **99**, 043506 (2019).

[59] N. Schöneberg, G. F. Abellán, A. P. Sánchez, S. J. Witte, V. Poulin, and J. Lesgourgues, The H_0 Olympics: A fair ranking of proposed models, Phys. Rep. **984**, 1 (2022).